energies

MDPI

Article

Well-Dispersed $ZnFe_2O_4$ Nanoparticles onto Graphene as Superior Anode Materials for Lithium Ion Batteries

Yiseul Park [1,*], Misol Oh [2] and Jae Hyun Kim [2]

[1] Department of Chemical Engineering, Pukyong National University, Yongso-ro 48513, Korea
[2] Smart Textile Convergence Research Group, Daegu Gyeongbuk Institute of Science and Technology (DGIST), Hyeonpung-myeon 42988, Korea; oms42@dgist.ac.kr (M.O.); jaehyun@dgist.ac.kr (J.H.K.)
* Correspondence: dewpark@pknu.ac.kr; Tel: +82-51-629-6432

Received: 28 November 2018; Accepted: 15 January 2019; Published: 18 January 2019

Abstract: We prepared well-dispersed $ZnFe_2O_4$ (ZFO) nanoparticles on a graphene sheet by a facile one-step hydrothermal method using glucose as a novel linker agent and low-cost graphene flake. It was found that the glucose linkage on graphene not only prevented the aggregation of ZFO particles, but also induced the exfoliation of graphene flakes. The addition of glucose during the synthesis made surface linkages on the graphene surface, and it reacted with ZFO precursors, resulting in the well-dispersed ZFO nanoparticles/graphene composite. Furthermore, the size distribution of the resultant composite particles was also shifted to the smaller particle size compared to the composite prepared without glucose. The newly prepared ZFO/graphene composite provided a higher lithium storage capability and cycle performance compared to the ZFO/graphene sample which was prepared without glucose. The good dispersion of ZFO nanoparticles on graphene and the small particle size of the composite led to markedly improved electrochemical performance. Its reversible discharge capacity was 766 mAh g^{-1} at 1 A g^{-1}, and it also maintained as 469 mAh g^{-1} at 6 A g^{-1}.

Keywords: $ZnFe_2O_4$; graphene; glucose; lithium ion battery

1. Introduction

Transition metal oxides are promising anode materials of lithium ion batteries due to their high reversible capacities [1,2]. Among them, Fe-based binary and ternary oxides have been explored as anode materials because of their feasibility to control energy density and working voltages by varying the transition metal content. $ZnFe_2O_4$ (ZFO) exhibits a lower working voltage to enhance the output voltage. It generates a high capacity by the formation of Li–Zn alloy during discharge [3–6]. However, it suffers from structural instability due to volume change during charge/discharge course, as well as low electron conductivity. To overcome its leakages, carbon materials (e.g., graphene, graphene oxides, carbon nanotubes, graphite, etc.) have been combined with ZFO [7–11]. Graphene has been widely used to improve the electrochemical properties of electrodes, as it has excellent conductivity and structural flexibility. That being said, it is an expensive material, and its price tends to limit its use in industrial applications. Although graphene flake (i.e., an aggregated form of graphene) is cheap, its electrochemical and physical properties are worse than those of a thin graphene sheet. However, aggregated graphene flakes could be easily expanded and exfoliated by a urea-assisted sonication treatment [12,13]. Therefore, this method was applied in this study to obtain cheap graphene sheets. In this study, exfoliated graphene flake was integrated into ZFO to overcome the poor electrical conductivity of ZFO. More importantly, glucose was added as a linker between

graphene and ZFO to prepare a well-dispersed ZFO/graphene composite. This was different from the ZFO/graphene composite prepared without glucose, which in the presence of glucose provided increased lithium storage capability and greatly improved electrochemical performance for lithium ion batteries. The detailed characteristics and electrochemical properties of the prepared composites are systematically studied in this paper.

2. Experimental

2.1. Preparation of Electrodes

All chemicals were used without any further purification in this experiment. $ZnFe_2O_4$/graphene (ZFO–G) was synthesized using the hydrothermal method. Firstly, aggregated graphene bulk flake was dispersed by sonication in a 2 wt% urea solution to prepare more expanded graphene flake with wider gaps between sheets. Then, 5 mmol $Zn(NO_3)_2$ and 10 mmol $Fe(NO_3)_2$ were dissolved in 40 mL of distilled water, and 15 mL of concentrated NaOH was added into the former solution. The graphene flake suspension was added to make 10 wt% of graphene in solution. The resulting solution was transferred into a Teflon-lined autoclave reactor (100 mL) and treated at 180 °C for 12 h. The collected precipitate was washed with distilled water and ethanol and dried at 60 °C for 24 h. For the $ZnFe_2O_4$/graphene prepared with glucose (ZFO–G–GL) sample, 0.9 g of glucose was also added into the above solution with the identical preparation procedure to ZFO–G. The synthesis illustration is shown in Figure 1. For comparison, the pure ZFO particles were prepared in the same way as described above, without the addition of graphene and glucose. For the preparation of the electrodes, a slurry was prepared by mixing synthesized samples, a super P conducting additive, and sodium carboxymethyl cellulose (CMC, 1.25 wt%) binder at a weight ratio of 75:20:5 with water as a solvent, using ball milling for 24 h at 100 rpm [10,11,14,15]. The prepared slurry was coated on copper foil and dried at 70 °C in a vacuum oven for 12 h to remove water. Then, it was pressed into a final thickness of 50–60 µm and cut into sections with 14-mm diameter. The average loading amounts of slurry on each electrode was 1.064 mg after drying.

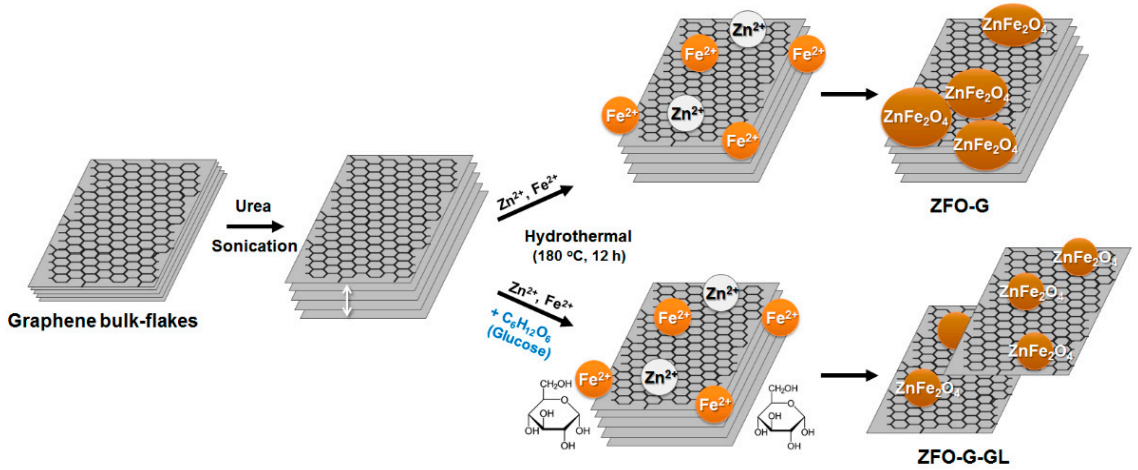

Figure 1. Preparation procedure of conventional $ZnFe_2O_4$/graphene (ZFO–G) and well-dispersed $ZnFe_2O_4$/graphene by using glucose (ZFO–G–GL).

2.2. Characterization

The crystal structures of the synthesized samples were studied by X-ray diffraction (XRD) analysis using an Empyrea X-ray diffractometer and Cu Kα radiation (2θ: 10–80°). Scanning electron microscopy (SEM) images of the samples were obtained using an FE-SEM system (S-4800, Hitachi) operated at 3 keV. An FE-TEM (HF-3300, Hitachi) was used to study the morphologies and nanostructures of the composites. The particle size distribution was measured using an electrophoretic

light scattering analyzer (Malvern). Electrochemical tests were carried out using CR2032 coin cells. The cells were assembled in an Ar-filled glove box with Li foil as the counter electrode, 1 M $LiPF_6$ in an ethylene carbonate (EC)/dimethyl carbonate (DMC) (3:7 by volume) as the electrolyte, and a polypropylene membrane as the separator. The charge/discharge tests were carried out using potentiostat (WBCS3000S, WONATECH) with the potential range of 0.01–3 V. Electrochemical impedance spectroscopy (EIS) was carried out in a frequency range of 1 MHz to 0.1 Hz using an electrochemical impedance analyzer (ZIVE SP1, WONATECH).

3. Results and Discussion

The prepared ZFO samples (ZFO, ZFO–G, and ZFO–G–GL) were investigated by means of XRD, SEM, HR–TEM, and size distribution analysis. Figure 2 presents XRD patterns of those samples. All major peaks were well-matched to the standard $ZnFe_2O_4$ diffraction peaks (JCPDS file no. 65-3111), and no impurities were observed in ZFO or ZFO–G samples. However, the ZFO–G–GL sample contained ZnO (JCPDS file no. 36-1451) as an impurity in the structure, which might be attributed to the larger contents of oxygen atoms that originated from the glucose addition during the preparation procedure.

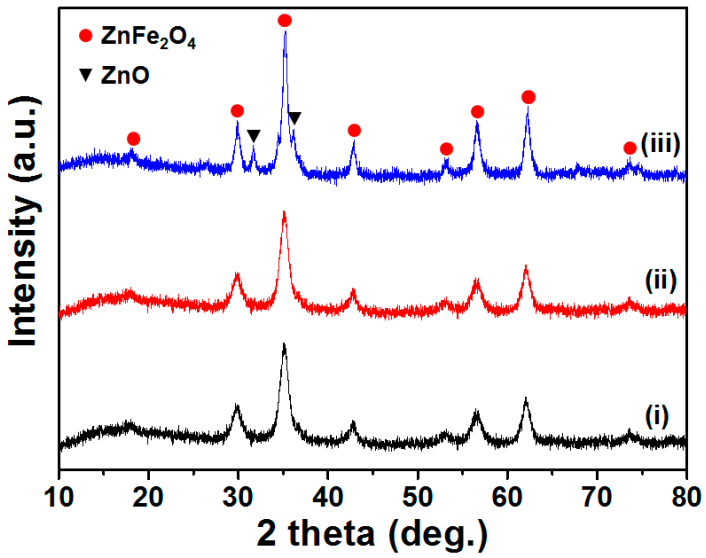

Figure 2. X-ray diffraction patterns of (i) ZFO, (ii) ZFO–G, (iii) ZFO–G–GL. The peaks corresponding to $ZnFe_2O_4$ and ZnO are labeled with circles and triangles, respectively.

In Figure 3, SEM images of those samples were compared. Pure ZFO nanoparticles (primary particle size <20 nm) were aggregated, each forming bigger particles. In the image of ZFO–G samples as shown in Figure 3b, the size of the ZFO nanoparticle was similar to that of pure ZFO samples, but the graphene flake particles were also observed. The morphology of graphene flakes was close to a spherical shape with the size of 300–500 nm, which implies that the exfoliation of the graphene flake by sonication in the urea solution was not successfully achieved. In contrast, the larger size of the graphene flakes disappeared in the ZFO–G–GL sample, but it showed that thinner graphene flakes were in more exfoliated states than in the ZFO–G samples. Furthermore, the separated graphene flakes could not be found in ZFO–G–GL samples, due to the good coverage of ZFO nanoparticles on the exfoliated graphene flakes that was attributed to the glucose, which acted as a linker between ZFO and graphene flakes.

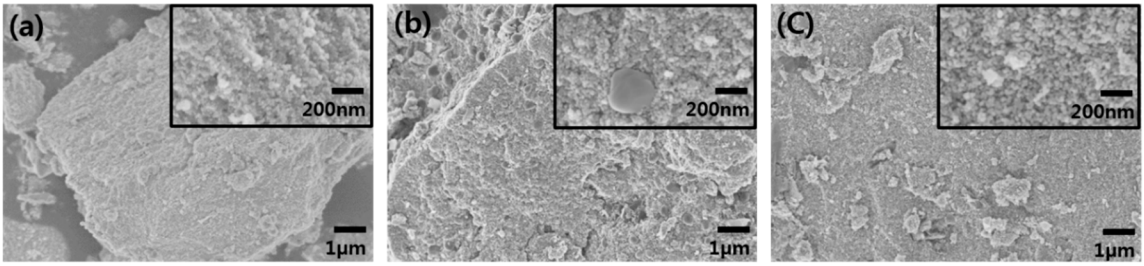

Figure 3. Scanning electron microscopy (SEM) images of (**a**) ZFO; (**b**) ZFO–G; and (**c**) ZFO–G–GL.

The TEM images of ZFO–G and ZFO–G–GL are compared in Figure 4. Unlike the ZFO–G sample (Figure 4a), well-dispersed ZFO nanoparticles were clearly observed in the ZFO–G–GL sample (Figure 4b). The EDX elemental mapping provided further evidence for the dispersion of ZFO nanoparticles on graphene in the presence of glucose. Furthermore, the aggregated graphene flakes were not easily observed in the ZFO–G–GL sample. This is consistent with the observation of its SEM image, where ZFO–G–GL showed good coverage of ZFO nanoparticles on graphene flakes (Figure 3c). Consequently, the addition of glucose during synthesis could not only prevent ZFO particle aggregation, but also lead to the exfoliation of graphene flakes. As we illustrated in Figure 1; Fe^{2+}, Zn^{2+} and glucose adsorbed onto the surface of graphene flakes, which have expanded gaps and oxidized states due to the urea pretreatment. Glucose was used to fix the seeds of ZFO onto graphene flakes to effectively hinder the aggregation of ZFO nanoparticles. When the glucose and Fe^{2+}, Zn^{2+} ions penetrate between the expanded gaps in graphene flakes, the linkage formation by glucose can induce an exfoliation of the aggregated graphene flakes by increasing the gap between graphene layers. Thus, the glucose molecules provide a linker on the graphene surfaces and promote the uniform growth of ZFO nanoparticles onto the graphene, resulting in the exfoliation of the aggregated graphene flakes and the formation of more uniform ZFO/graphene composites.

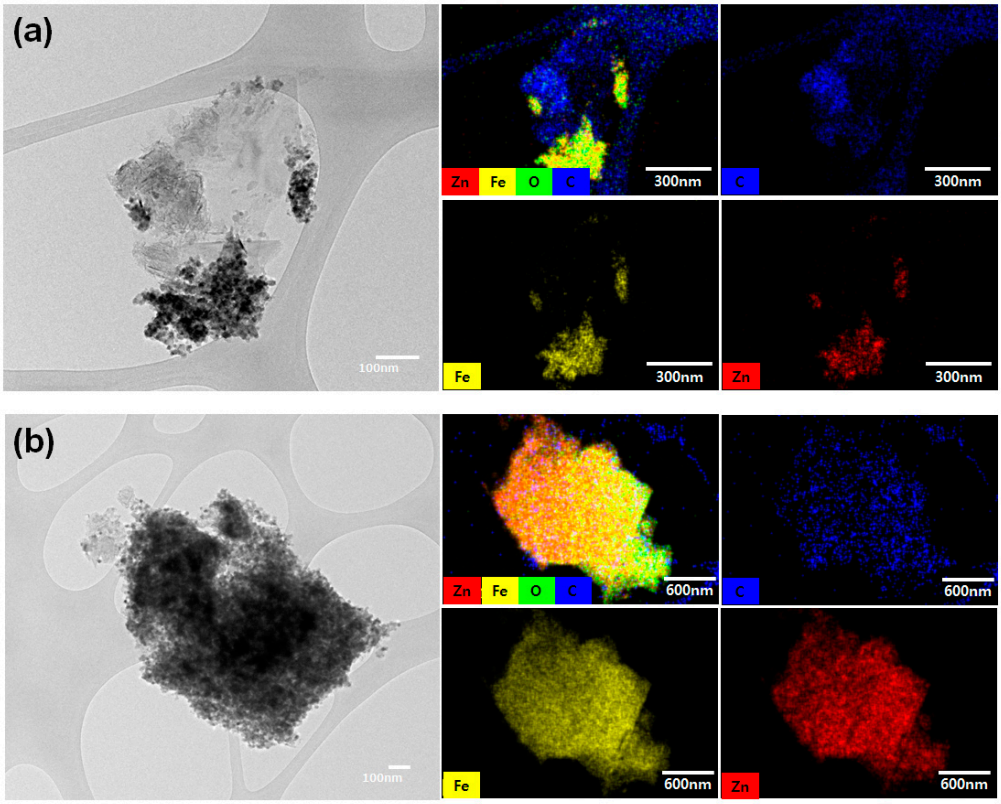

Figure 4. TEM images and elemental map of (**a**) ZFO–G; (**b**) ZFO–G–GL.

Well-dispersed ZFO particles on graphene and the further exfoliation in ZFO–G–GL samples could be confirmed by comparing particle size distribution with that of the ZFO–G sample. In Figure 5a,b, the suspension and precipitation of ZFO, ZFO–G, and ZFO–G–GL were compared. ZFO and ZFO–G–GL showed good suspension right after shaking, but ZFO–G particles started to precipitate quickly right after shaking. After 5 min, the stable suspension of ZFO–G–GL was well maintained, but significantly more ZFO and ZFO–G particles were precipitated. The particle size distributions of samples were also measured using an electrophoretic light scattering (ELS) analyzer, as shown in Figure 5c. It was found that the ZFO–G–GL samples consisted of much smaller particles compared to ZFO–G, showing a size distribution in a range of 50–400 nm. The size distribution showed a decrease in the particle size in the ZFO–G–GL sample compared to the ZFO–G sample.

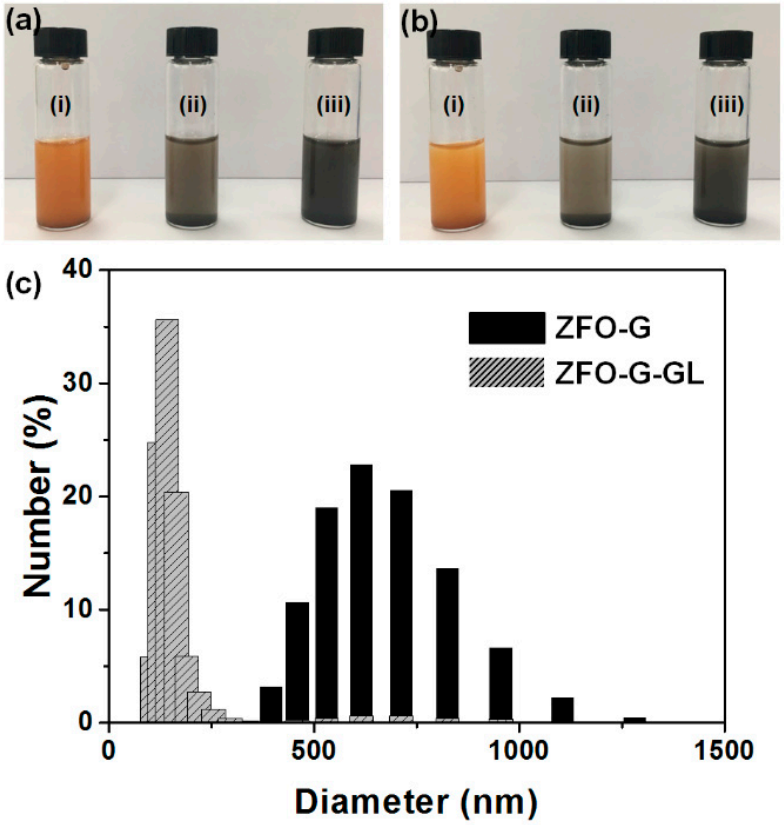

Figure 5. Suspension of (i) ZFO, (ii) ZFO–G, (iii) ZFO–G–GL in water (**a**) right after a shaking; (**b**) formation of precipitations after 5 min; and (**c**) particle size distribution of ZFO–G and ZFO–G–GL.

Figure 6 shows the initial discharge/charge curves for graphene flakes, ZFO, ZFO–G, and ZFO–G–GL electrodes for the first five cycles at 1 A g^{-1} in the potential range from 0.01 to 3.0 V with Li foil as a counter electrode. As control experiments, the discharge/charge curves were obtained for the exfoliated graphene and ZFO. The initial discharge capacity of the graphene and ZFO were 130 and 350 mAh g^{-1}, respectively. However, the discharge capacity of ZFO exhibited drastic decay after the first cycle. The observed initial irreversible capacity loss of the samples was probably because of the formation of a solid electrolyte interface (SEI) on the surface of electrodes during the first lithium insertion process [14,15]. Although the graphene addition increased the specific capacity in the ZFO–G results (Figure 6c), the enhancement was not significant and the stability was still low. On the other hand, the ZFO–G–GL electrode exhibited a high reversible current capacity of 821 mAh g^{-1}, without the loss of capacity for five cycles. This is shown in Figure 6d. The normalized differential capacity (1/Q(dQ/dV)) plots of ZFO–G and ZFO–G–GL for the initial five cycles are shown in Figure 7. At a plateau around 0.75 V, the high reversible capacity in the first cycle could be explained by the formation of a SEI, which consumes many lithium ions [11]. Plateaus were also

observed around 1.0 and 1.6 V, respectively, and corresponded to the reversible redox reactions during lithium insertion/extraction [15]. Figure 7a shows the voltage change in ZFO–G electrodes during the lithiation and delithiation for five cycles. On the other hand, the voltage shift in the ZFO–G–GL electrode was negligible compared to the ZFO–G electrode, which implies the stable status of the ZFO–G–GL electrode during the cycles due to a lower resistance [16,17].

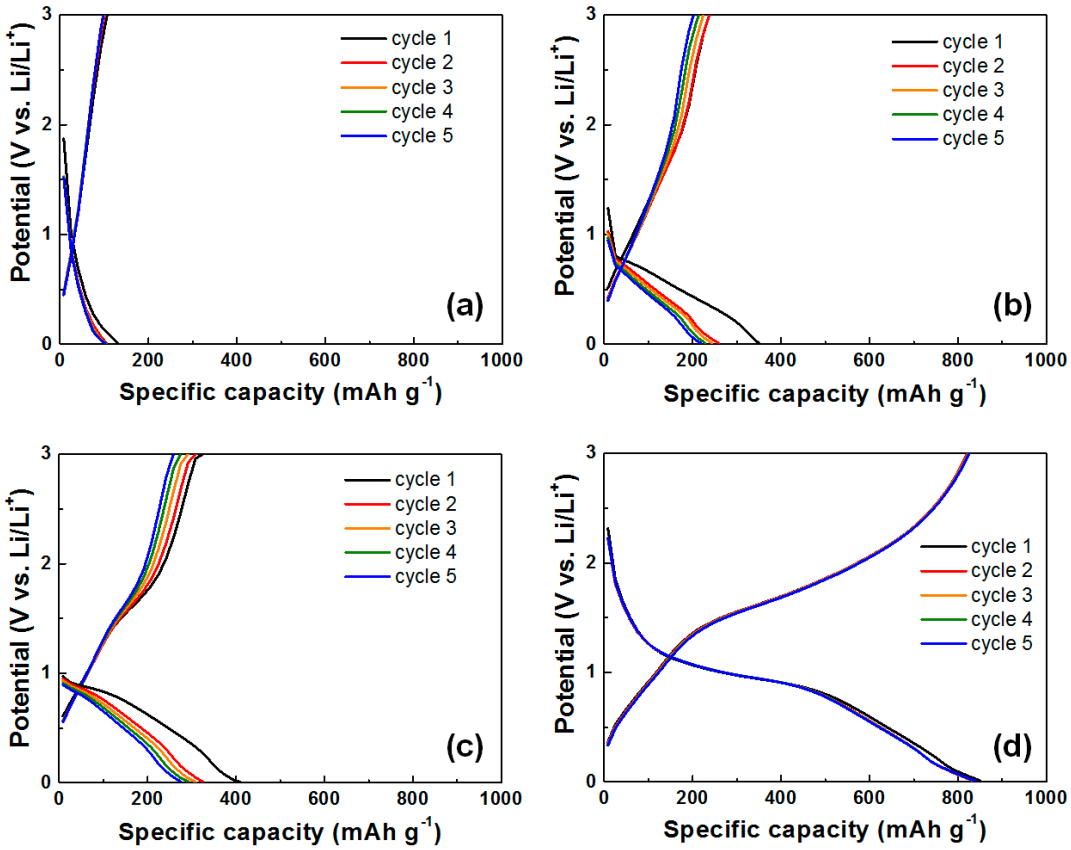

Figure 6. Discharge/charge curves of (**a**) graphene; (**b**) ZFO; (**c**) ZFO–G; and (**d**) ZFO–G–GL for the first five cycles at a current density of 1 A g^{-1}.

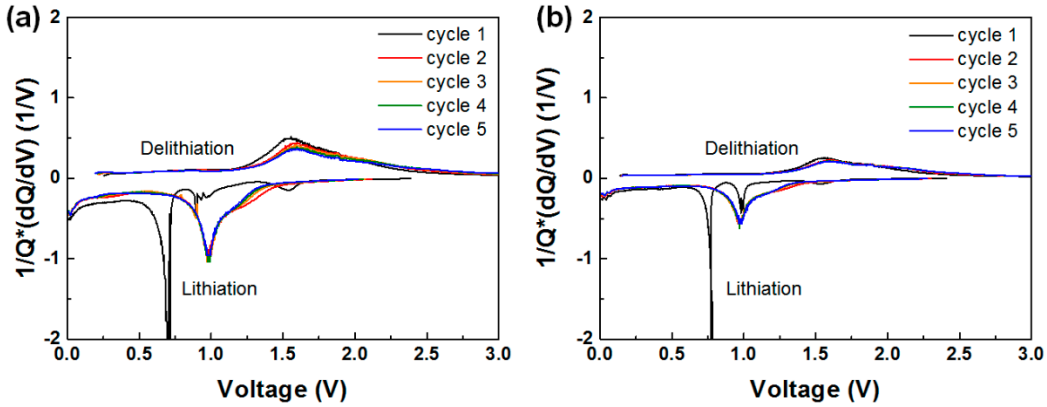

Figure 7. Normalized differential capacity plots of (**a**) ZFO–G and (**b**) ZFO–G–GL for the first five cycles at a current density of 1 A g^{-1}.

Electrochemical impedance spectra for electrodes are shown in Figure 8a. The impedance spectra consisted of a high-frequency semicircle and a low-frequency tail, attributed to the electrode-electrolyte interfacial charge transfer impedance (R_{ct}) and the diffusion-controlled Warburg impedance (Z_w), respectively. ZFO–G exhibited lower interfacial impedance compared with ZFO, but the decrease of resistance in ZFO–G–GL was more significant than that of ZFO. This result is consistent with the discharge/charge capacity tendency shown in Figure 6 and the observation that ZFO–G–GL electrodes showed no obvious plateau reductions or peak shifting in Figure 7b. Figure 8b shows the cycling performances at different current densities (i.e., at 0.2, 0.5, 1, 2, 4, and 6 A g^{-1}). The pure graphene flake and ZFO electrodes exhibited fast capacity degradation, with its specific capacity being 102 mAh g^{-1} and 265 mAh g^{-1} at 1 A g^{-1}, respectively. This fading of their capacity can be explained by their poor structural stability due to the large volume change induced by the Li ions insertion/extraction during cycling. Additionally, the low electrochemical conductivity of ZFO was responsible for the reduction of capacity with cycles. Although ZFO–G electrodes exhibited a higher specific capacity (532 mAh g^{-1} at 1 A g^{-1}) than that of pure graphene and ZFO, the capacity drastically decreased as the current density increased. The capacity of ZFO–G at the final five cycles at 0.5 A g^{-1} was not fully recovered to the capacity obtained at the previous cycles with 0.5 A g^{-1}, which indicates that ZFO–G electrodes contained irreversible reactions during the charging/discharging processes, reducing their capacity. Compared with other electrodes, ZFO–G–GL exhibited higher reversible capacity and improved rate capability, as given in Figure 8b. The specific capacity of ZFO–G–GL at 1 A g^{-1} was 766 mAh g^{-1}, and notably, it was maintained as 469 mAh g^{-1} even at 6 A g^{-1}. This significant improvement of capacity and stability of ZFO–G–GL is attributed to the good dispersion of ZFO on graphene with increasing electrode conductivity. Additionally, the presence of a small amount of ZnO in ZFO–G–GL can improve electrochemical performance by enhancing the electrical conductivity and chemical-thermal stability due to the hetero-junction formation, thereby improving its rate capability [18]. To evaluate the cyclic stability of samples, they were further charged/discharged at a current rate of 1 A g^{-1} for 200 cycles, as shown in Figure 8c. The specific capacities of ZFO and ZFO–G samples drastically decreased with the increase of cycles due to the SEI instability and structural change of ZFO during lithium insertion/extraction [14]. That of ZFO–G–GL also decreased until it reached 50 cycles. However, it increased again after about 50 cycles with recovering capacity. It seems to be due to the formation of a polymeric gel-like film on the electrode resulting from kinetically activated electrolyte degradation, as normally observed for transition metal oxide-based anodes [19,20].

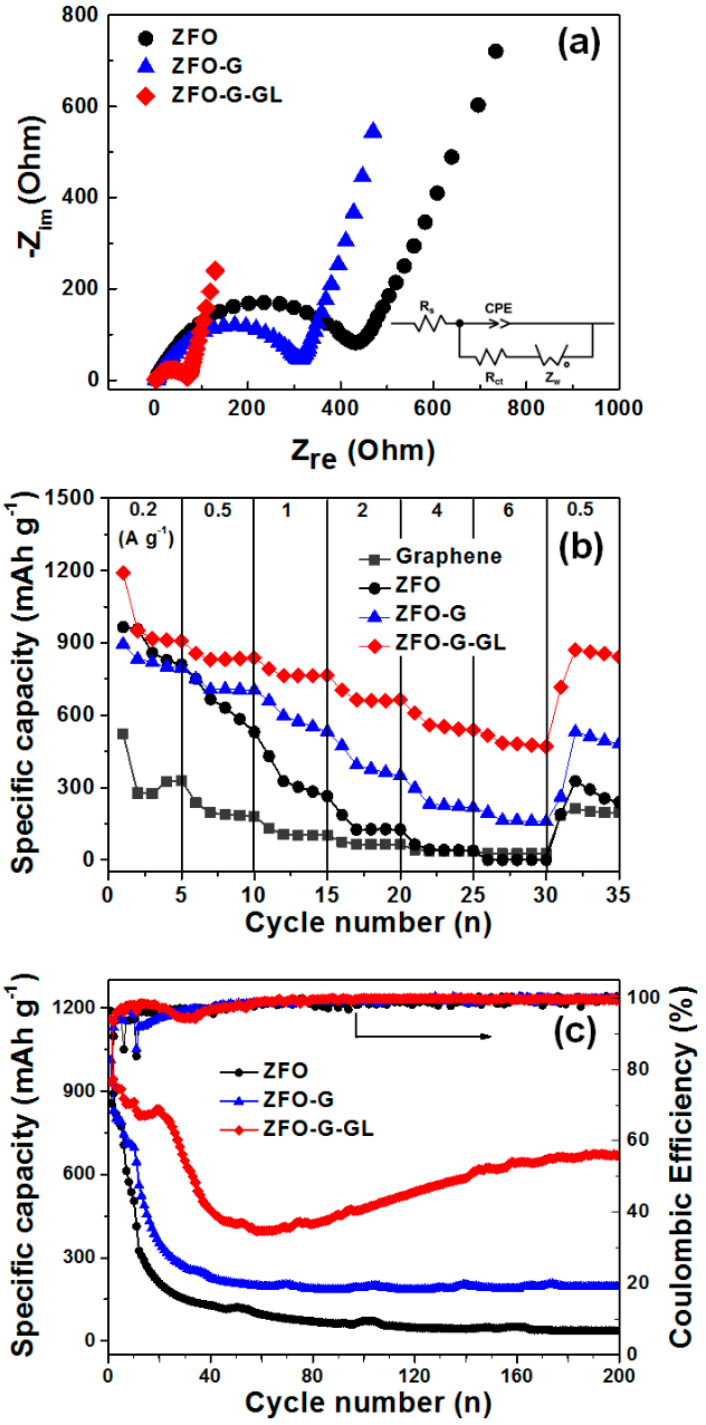

Figure 8. (**a**) Electrochemical impedance spectra (inset) equivalent circuit; (**b**) specific discharge capacities at various current density (0.2–6 A g^{-1}); and (**c**) cycling performances and coulombic efficiency at a rate of 1 A g^{-1} of ZFO, ZFO–G, ZFO–G–GL, and graphene (only in (b)).

4. Conclusions

In summary, we prepared well-dispersed ZFO on graphene through a facile one-step hydrothermal process using glucose as a linker agent and a low-cost graphene flake as a source of graphene sheets. The utilization of glucose during the hydrothermal process not only prevented the aggregation of ZFO particles, but also led to the exfoliation of graphene flakes. The well-dispersed structure of ZFO/graphene composites were responsible for the improved surface lithium storage

reaction and conductivity, which resulted in significantly improved reversible capacity and rate capability.

Author Contributions: Conceptualization, Y.P.; Investigation, M.O. and J.H.K.; Supervision, Y.P.; Writing—original draft, Y.P.; Writing—review & editing, Y.P.

Funding: This work was supported by the National Research Foundation of Korea (NRF) grant (No. 2017R1C1B2011147) and DGIST R&D program (17-NT-02) funded by the Korea government (MSIT) and the Korea Institute of Energy Technology Evaluation and Planning (KETEP) and the Ministry of Trade, Industry & Energy (MOTIE) of the Republic of Korea (No. 20174010201460).

Conflicts of Interest: The authors declare no conflict of interest.

References

1. Poizot, P.; Laruelle, S.; Grugeon, S.; Dupont, L.; Tarascon, J.M. Nano-sized transition-metal oxides as negative-electrode materials for lithium-ion batteries. *Nature* **2000**, *407*, 496–499. [CrossRef] [PubMed]
2. Zhang, L.; Wu, H.B.; Lou, X.W. Iron-oxide-based advanced anode materials for lithium-ion batteries. *Adv. Energy Mater.* **2014**, *4*, 1300958. [CrossRef]
3. Ding, Y.; Yang, Y.; Shao, H. High capacity $ZnFe_2O_4$ anode material for lithium ion batteries. *Electrochim. Acta* **2011**, *56*, 9433–9438. [CrossRef]
4. Guo, X.; Lu, X.; Fang, X.; Mao, Y.; Wang, Z.; Chen, L.; Xu, X.; Yang, H.; Liu, Y. Lithium storage in hollow spherical $ZnFe_2O_4$ as anode materials for lithium ion batteries. *Electrochem. Commun.* **2010**, *12*, 847–851. [CrossRef]
5. Teh, P.F.; Sharm, Y.; Pramana, S.S.; Srinivasan, M. Nanoweb anodes composed of one-dimensional, high aspect ratio, size tunable electrospun $ZnFe_2O_4$ nanofibers for lithium ion batteries. *J. Mater. Chem.* **2011**, *21*, 14999–15008. [CrossRef]
6. Xu, H.; Chen, X.; Chen, L.; Li, L.E.; Xu, L.; Yang, J.; Qian, Y. A comparative study of nanoparticles and nanospheres $ZnFe_2O_4$ as anode material for lithium ion batteries. *Int. J. Electrochem. Sci.* **2012**, *7*, 7976–7983.
7. Deng, Y.; Zhang, Q.; Tang, S.; Zhang, L.; Deng, S.; Shi, Z.; Chen, G. One-pot synthesis of $ZnFe_2O_4$/C hollow spheres as superior anode materials for lithium ion batteries. *Chem. Commun.* **2011**, *47*, 6828–6830. [CrossRef] [PubMed]
8. Sui, J.; Zhang, C.; Hong, D.; Li, J.; Cheng, Q.; Li, Z.; Cai, W. Facile synthesis of MWCNT–$ZnFe_2O_4$ nanocomposites as anode materials for lithium ion batteries. *J. Mater. Chem.* **2012**, *22*, 13674–13681. [CrossRef]
9. Varzi, A.; Bresser, D.; Zamory, J.V.; Müller, F.; Passerini, S. $ZnFe_2O_4$ -C/$LiFePO_4$ -CNT: A novel high-power lithium-ion battery with excellent cycling performance. *Adv. Energy Mater.* **2014**, *4*, 1400054. [CrossRef] [PubMed]
10. Bresser, D.; Paillard, E.; Kloepsch, R.; Krueger, S.; Fiedler, M.; Schmitz, R.; Baither, D.; Winter, M.; Passerini, S. Carbon coated $ZnFe_2O_4$ nanoparticles for advanced lithium-ion anodes. *Adv. Energy Mater.* **2013**, *3*, 513–523. [CrossRef]
11. Yao, X.; Kong, J.; Zhou, D.; Zhao, C.; Zhou, R.; Lu, X. Mesoporous zinc ferrite/graphene composites: Towards ultra-fast and stable anode for lithium-ion batteries. *Carbon* **2014**, *79*, 493–499. [CrossRef]
12. He, P.; Zhou, C.; Tian, S.; Sun, J.; Yang, S.; Ding, G.; Xie, X.; Jiang, M. Urea-assisted aqueous exfoliation of graphite for obtaining high-quality graphene. *Chem. Commun.* **2015**, *51*, 4651–4654. [CrossRef] [PubMed]
13. Cho, S.-J.; Choi, K.-H.; Yoo, J.-T.; Kim, J.-H.; Chun, S.-J.; Park, S.-B.; Choi, D.-H.; Wu, Q.; Lee, S.-Y.; Lee, S.-Y. Hetero-nanonet rechargeable paper batteries: Toward ultrahigh energy density and origami foldability. *Adv. Funct. Mater.* **2015**, *25*, 6029–6040. [CrossRef]
14. Hoe, L.; Lian, L.; Zhang, L.; Pang, G.; Yuan, C.; Zhang, X. Self-sacrifice template fabrication of hierachical mesoporous bi-component-active ZnO/$ZnFe_2O_4$ sub-microcube as superior anode towards high-performance lithium-ion battery. *Adv. Funct. Mater.* **2015**, *25*, 238–246. [CrossRef]
15. Zhong, X.-B.; Jin, B.; Yang, Z.-Z.; Wang, C.; Wang, H.-Y. Facile shape design and fabrication of $ZnFe_2O_4$ as an anode material for Li-ion batteries. *RSC Adv.* **2014**, *4*, 55173–55178. [CrossRef]
16. Lee, E.; Park, J.S.; Wu, T.; Sun, C.-J.; Kim, H.; Stair, P.C.; Lu, J.; Zhou, D.; Johnson, C.S. Role of Cr^{3+}/Cr^{6+} redox in chromium-substituted Li_2MnO_3 $LiNi_{1/2}Mn_{1/2}O_2$ layered composite cathodes: Electrochemistry and voltage fade. *J. Mater. Chem. A* **2015**, *3*, 9915–9924. [CrossRef]

17. Huang, Q.; Loveridge, M.J.; Genieser, R.; Lain, M.J.; Bhagat, R. Electrochemical evaluation and phase-related impedance studies on silicon–few layer graphene (FLG) composite electrode systems. *Sci. Rep.* **2018**, *8*, 1386. [CrossRef] [PubMed]
18. Pan, P.; Wang, T.; Chen, L.; Wang, F.; Yang, X.; Qin, C.; Ding, Y. Crystal-seeds induced construction of ZnO-$ZnFe_2O_4$ micro-cubic composites as excellent anode materials for lithium ion battery. *RSC Adv.* **2018**, *8*, 16187–16192. [CrossRef]
19. Grugeon, S.; Laruelle, S.; Dupont, L.; Tarascon, J.-M. An updateon the reactivity of nanoparticles Co-based compounds towards Li. *Solid State Sci.* **2003**, *5*, 895–904. [CrossRef]
20. Zou, F.; Hu, X.; Li, Z.; Qie, L.; Hu, C.; Zeng, R.; Jiang, Y.; Huang, Y. MOF-derived porous ZnO/$ZnFe_2O_4$/C octahedra with hollow interiors for high-rate lithium-ion batteries. *Adv. Mater.* **2014**, *26*, 6622–6628. [CrossRef] [PubMed]